Supplementary Information (SI) for Inorganic Chemistry Frontiers.

Supporting Information

Tailoring Electronic Structure and Kinetics of VSe_2 via Selenium Vacancy Engineering for Ultralong-Life Zinc-Ion Batteries

Dejun Gong[a], Yuling Tu[a], Lirong Jia[a], Zeming Lu[a], Jun Gao[a], Hui Chai[a*], Yali Cao[a], Xiaogang Zhang[b*], Naseem Iqbal[c]

[a]State Key Laboratory of Chemistry and Utilization of Carbon Based Energy Resources; Key Laboratory of Energy Materials Chemistry, Ministry of Education; College of Chemistry, Xinjiang University, Urumqi, 830017, Xinjiang, PR China

[b]College of Material Science and Engineering, Nanjing University of Aeronautics and Astronautics, Yudao Street 29, Nanjing 210016, PR China

[c]US-Pakistan Centre for Advanced Studies in Energy, National University of Sciences and Technology (NUST), H-12, Islamabad 44000, Pakistan

*Corresponding author: Tel: +86 9918583083; Fax: +86 9918588883; E-mail: huichmails@163.com

Experimental Section

Materials

All reagents were of analytical grade and used without further purification. Ammonium metavanadate (NH_4VO_3), selenium dioxide (SeO_2), and oxalic acid dihydrate ($C_2H_2O_4\cdot 2H_2O$) were purchased from Aladdin Reagent Company (China).

Synthesis of VSe_2 electrode material

First, 2 mmol NH_4VO_3, 4 mmol SeO_2, and 20 mmol $C_2H_2O_4\cdot 2H_2O$ were dissolved in 25 mL of deionized (DI) water under stirring. After stirring for 1 h, the mixture was transferred into a 50 mL Teflon-lined autoclave and heated to 200 °C for 24 h. Following natural cooling, the black product was collected, washed three times with

---

*Corresponding author: Tel: +86 991 858 3083; Fax: +86 991 858 8883; E-mail:huichmails@163.com ethanol and DI water, respectively, and vacuum-dried at 60 °C for 10 h to yield VSe_2.

Synthesis of Se-Vacancy-Rich VSe_{2-x}-40 and other comparative electrode materials

Typically, 0.2 g of the as-synthesized VSe_2 was dispersed in 25 mL of a 40 wt% hydrazine hydrate aqueous solution and stirred for 6 h. The VSe_{2-x}-40 sample was obtained by filtration, washing, and drying. To investigate the effect of hydrazine hydrate concentration, VSe_{2-x}-20 and VSe_{2-x}-60 were prepared under identical conditions by varying the concentration of the hydrazine hydrate solution to 20 wt% and 60 wt%, respectively.

Electrochemical measurements

The working electrode slurry was prepared by mixing the active material (70 wt%), Ketjen carbon black (20 wt%), and polyvinylidene fluoride (PVDF, 10 wt%) in the solvent N-methyl-2 pyrrolidone (NMP). Then, the slurry was spread onto the stainless-steel mesh, and the electrode was dried in a vacuum oven at 60 °C for 12 hours. The final electrode has a mass loading of approximately 1.0 mg cm^{-2}. The CR2032 type coin cells were assembled in air to investigate the electrochemical performance of the cathode materials. Use 3 M $ZnSO_4$ aqueous solution, glass fiber membrane and zinc foil as electrolyte, separator and anode. The LAND Battery Test System (CT2001A) performs galvanostatic charge/discharge (GCD) testing over a voltage range of 0.2 to 1.6 V. Cyclic voltammetry (CV) and electrochemical impedance spectroscopy (EIS) measurements were performed on an electrochemical workstation (CHI760E). All the above tests were performed at room temperature. Continuous constant current charge and discharge measurements and galvanostatic intermittent titration technology (GITT) experiments at voltages from 0.2 to 1.6V (vs. Zn/Zn^{2+}) were performed on a LAND battery test system (CT2001A).

Materials Characterization

X-ray diffraction (XRD) measurements were carried out on a Bruker D8 Advance X-ray diffractometer with a Cu Kα source (λ = 1.5406 Å). The morphology and components of the samples were obtained through a field emission scanning electron microscope (SEM, Hitachi S-4800) equipped with an energy dispersive spectrometer

(EDS) and transmission electron microscopy (TEM) with a JEOL JEM-2800. Raman spectra were measured by a Bruker Senterra R200-L spectrometer (532 nm). The electronic states of the samples were investigated by the Xray photoelectron spectroscopy (XPS, Thermo Fisher Scientific K-Alpha with Al Kα radiation). All binding energies were calibrated by the C 1s peak at 284.8 eV. Electron paramagnetic resonance (EPR) measurements (Bruker E500) were conducted in the X-band. X-ray absorption fine structure (XAFS) spectroscopy was carried out using the Rapid XAFS 2M (Anhui Absorption Spectroscopy Analysis Instrument Co. Ltd.) by transmission mode at 12 kV and 12 mA, and the Ge (211) spherically bent crystal analyzer with a radius of curvature of 500 mm was used for sample. Nitrogen adsorption-desorption isotherms were obtained using a gas adsorption analyzer (BET, ASAP2460) for Surface Area and Pore Porosimeter measurements. Nitrogen adsorption-desorption isotherms were recorded on a Micromeritics ASAP 2460 analyzer at -195.8 °C. The specific surface area was calculated using the Brunauer-Emmett-Teller (BET) method. The pore size distributions were derived from the desorption branch of the isotherms using the Barrett-Joyner-Halenda (BJH) model based on the Halsey thickness equation. Water contact angle measurements were performed using a Dataphysics OAC 25 instrument.

Computational Details

The DFT calculations in this work were performed using the Vienna Ab initio Simulation Package (VASP). The electron-ion interactions were described by the projector-augmented wave (PAW) method, and the exchange-correlation functional was treated within the generalized gradient approximation (GGA) using the Perdew-Burke-Ernzerhof (PBE) formalism, with dispersion corrections applied using the DFT-3 method. A plane-wave basis set with an energy cutoff of 400 eV was employed. The Brillouin zone was sampled with appropriate Γ-centered k-meshes (3×3×5), and the convergence criteria for energy and forces were set to 1×10^{-5} eV and 0.01 eV $Å^{-1}$, respectively. The climbing image-nudged elastic band (CI-NEB) method was utilized to locate the minimum energy path and the transition states for Zn^{2+} migration between stable sites.

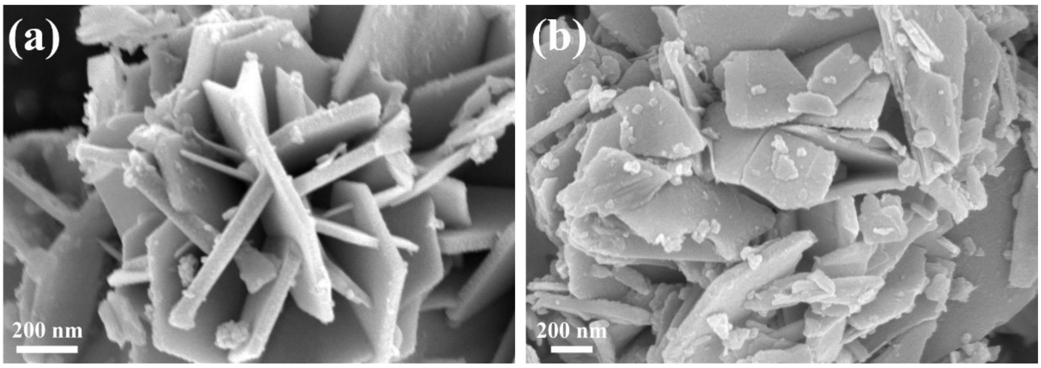

Fig.S1 SEM images of VSe_{2-x}-20 (a) and VSe_{2-x}-60 (b).

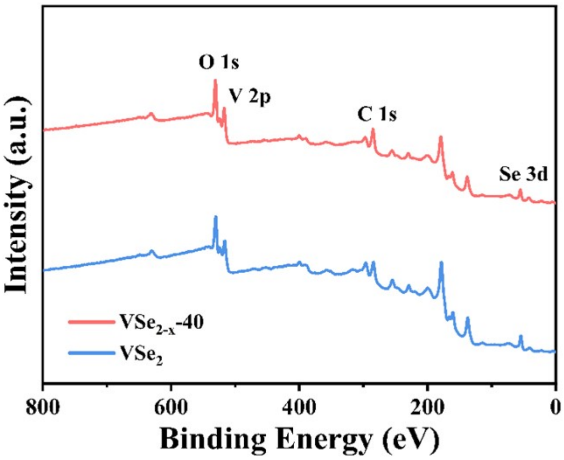

Fig. S2 XPS full spectra of VSe_2 and VSe_{2-x}-40.

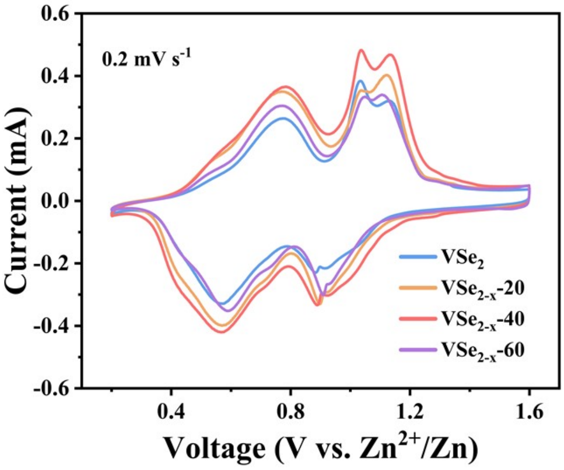

Fig. S3 CV curves for VSe_2, VSe_{2-x}-20, VSe_{2-x}-40, and VSe_{2-x}-60 at 0.2 mV s^{-1}.

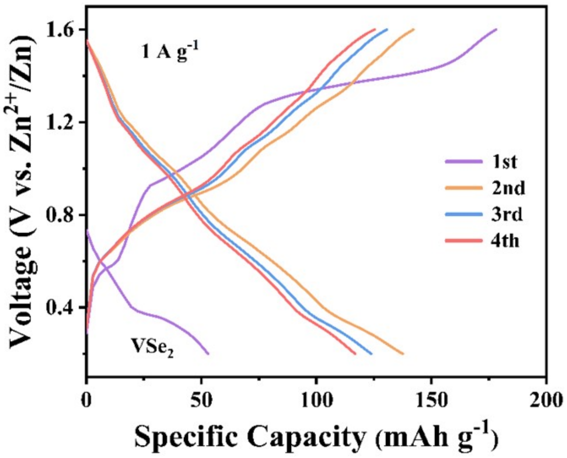

Fig. S4 The GCD curves of VSe_2 electrode at 1 A g^{-1}.

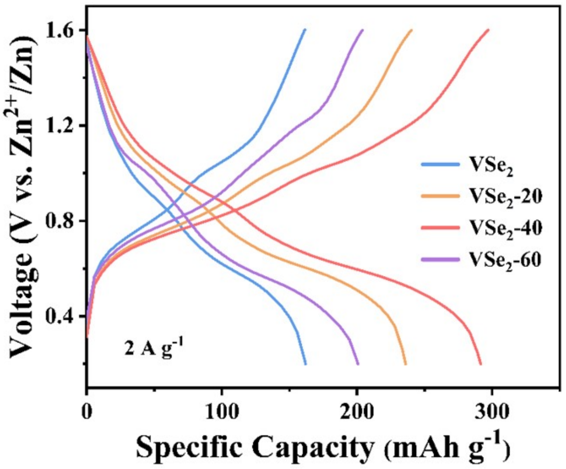

Fig. S5 The GCD curves of VSe_2, VSe_{2-x}-20, VSe_{2-x}-40 and VSe_{2-x}-60 electrodes at 2 A g^{-1}.

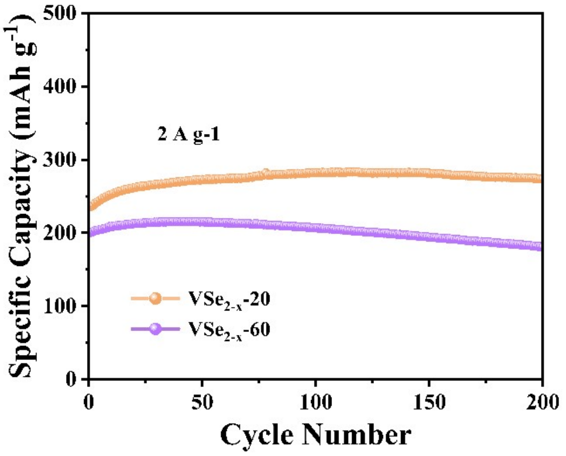

.

Fig. S6 Cycling stability of VSe_{2-x}-20 and VSe_{2-x}-60 electrodes at 2 A·g^{-1}.

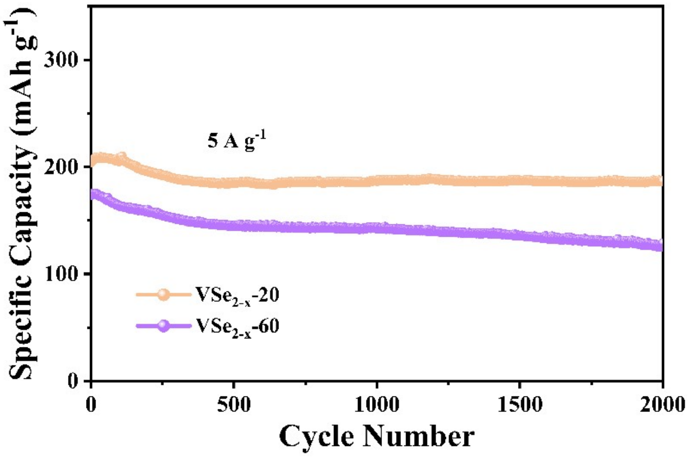

Fig. S7 Cycling stability of VSe$_{2-x}$-20 and VSe$_{2-x}$-60 electrodes at 2 A·g^{-1}.

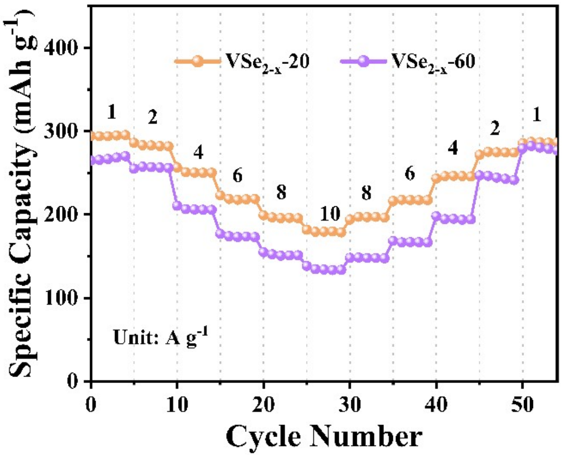

Fig. S8 The rate capabilities of VSe$_{2-x}$-20 and VSe$_{2-x}$-60 electrodes.

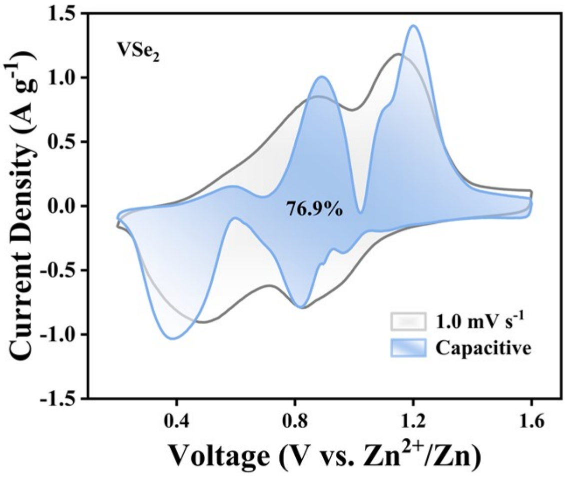

Fig. S9 Capacitive-controlled contribution at 1 mV s^{-1} of VSe$_2$

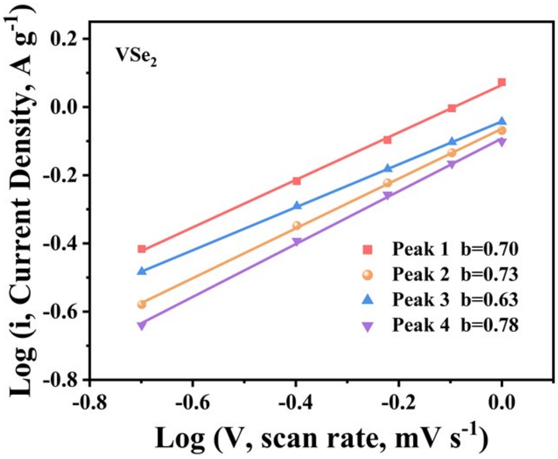

Fig. S10 The b values of VSe$_2$

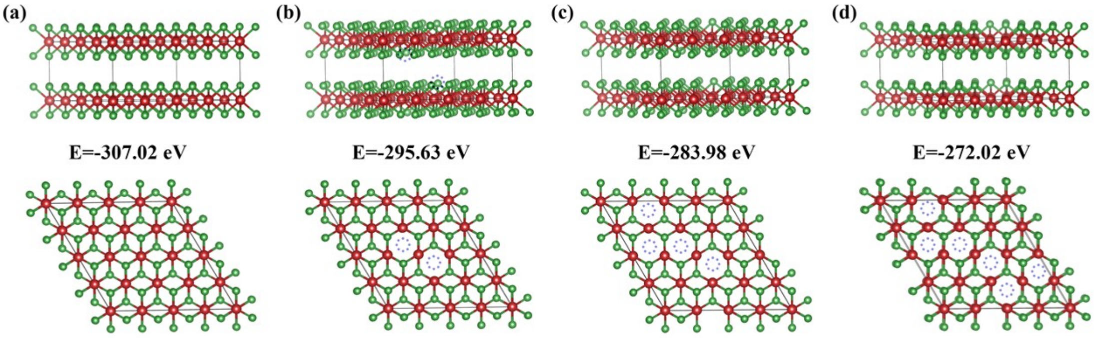

Fig. S11 The structural configurations of VSe$_2$ and the corresponding energy of the system (a) perfect VSe$_2$, (b) VSe$_{2-x}$ with low Se defect content, (c) VSe$_{2-x}$ with middle Se defect content, (d) VSe$_{2-x}$ with high Se defect content. (The green and red spheres represent the elements Se and V, respectively.)

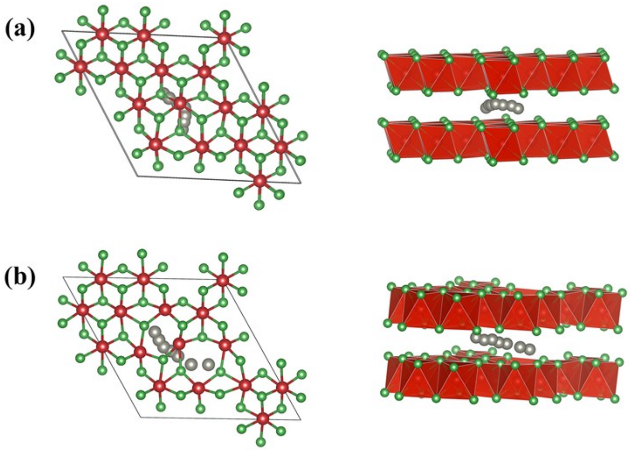

Fig. S12 Top view and side view of the optimal diffusion pathway of Zn^{2+} (a) VSe$_2$ and (b) VSe$_{2-x}$. (The green, red and grey spheres represent the elements Se, V and Zn, respectively.)

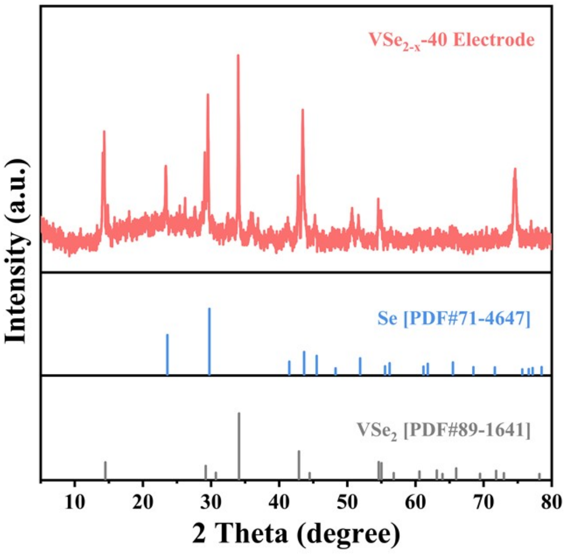

Fig. S13 XRD pattern of VSe$_{2-x}$-40 electrode.